Contents lists available at ScienceDirect

Journal of CO2 Utilization

LDH-derived CoTiAl mixed oxide as catalyst for photo-assisted CO2 hydrogenation

Manuel Molina-Muriel [a,b], Yong Peng [a], Horatiu Szalad [a], Antonio Ribera [b,*], Hermenegildo García [a,*]

[a] *Instituto de Tecnología Química CSIC-UPV, Universitat Politècnica de València and Consejo Superior de Investigaciones Científicas, Universitat Politècnica de València, Av. de los Naranjos s/n, Valencia 46022, Spain*
[b] *Departamento de Química Inorgánica, Universitat de València, Carrer del Doctor Moliner 50, Burjassot 46100, Spain*

A B S T R A C T

A layered double hydroxide (LDH) has been used as precursor for the synthesis of a multimetallic mixed oxide with photocatalytic activity. Thus, a trimetallic CoTiAl LDH has been synthesized as spherical aggregates of nanosheets. Analysis at short synthesis times indicates that CoTiAl-LDH particles grow perpendicular to initially formed oligomeric Ti-lactate nuclei. Calcination of CoTiAl-LDH at 400 °C affords the corresponding CoTiAl mixed oxide (MO) with low crystallinity having a cobaltite structure, while also maintaining the morphology. This CoTiAl-MO exhibits at 200 °C photocatalytic activity for CO_2 hydrogenation to CO, accompanied with lesser amounts of CH_4, with remarkable apparent quantum yields at 365 nm of 7.0 and 4.6 for CO and CH_4, respectively and very low apparent activation energy for 10 kJ/mol. The present results show a promising direction to exploit the potential that the preparation of multimetallic LDH offers for the synthesis of mixed oxides with optimal compositions for an even more enhanced photocatalytic activity.

1. Introduction

One of the possible strategies to decrease atmospheric CO_2 emissions is its capture and utilization, converting it into fuels and chemicals [1–3]. Due to the high thermodynamic stability, most of the chemical reactions involving CO_2 are highly endothermic, requiring energy to occur and making the reaction equilibrium highly unfavorable [4,5]. Among the few exceptions, CO_2 hydrogenation can be an exothermic reaction depending on the products formed and, therefore, can be performed at high CO_2 product yields compared to other alternative processes [6]. However, even if thermodynamically allowed, CO_2 hydrogenation processes exhibit extremely slow kinetics and considerable activation energy is required to overcome kinetic barriers [7]. While thermocatalytic CO_2 hydrogenations are known since the early years of the 20th century, the current focus on renewable energies and particularly green electricity and natural sunlight has encouraged the use of electric potential or photons to promote CO_2 conversion [8–13]. Photocatalytic selective CO_2 hydrogenation has been reported with different photocatalysts including noble metals [14–16], there being an interest in developing efficient photocatalysts that contain abundant

first row transition metals, such as oxides, phosphates, or nitrides [17–20].

It is quite common that the photocatalytic activity of metallic oxides increases when more than one metal is present in the composition [21, 22]. Thus, it can be expected that the photocatalytic activity of trimetallic mixed oxides is increased compared to bimetallic or monometallic oxides. Given the general photocatalytic activity of Ti oxides [23–25], this element could be one of the three metals present in a trimetallic composite with expected photocatalytic properties, while others with hydrogenation activity, such as Co, being also very convenient. Other metals, like Al, could have a structural role, making possible the synthesis of a material precursor that eventually will render the multimetallic mixed oxide.

One general way to prepare mixed metal oxides of di and trivalent metal cations uses layered double hydroxides (LDH) as precursors [26, 27]. Although much less common, LDH can also be used as precursors of titanium-containing mixed oxides [28]. Here in, the preparation of a trimetallic Co, Ti and Al mixed oxide obtained from the corresponding LDH has been performed and its photocatalytic activity for CO_2 hydrogenation studied. It will be shown that this trimetallic mixed oxide

containing titanium exhibits a remarkable photocatalytic activity at temperatures in which the thermal catalytic activity is negligible with apparent quantum yields over 5% in the UV and with very low apparent activation energy values about 10 kJ/mol in this temperature range.

2. Materials and methods

2.1. Materials

Co$(NO_3)_2 \cdot 6 H_2O$, Al$(NO_3)_3 \cdot 9 H_2O$, Ti(IV) bis(ammonium lactate) dihydroxide and 10 wt% perfluorinated Nafion® resin solution were purchased from Sigma-Aldrich. Urea (99%) was obtained from Honeywell. Anhydrous Na$_2$SO$_4$ was purchased from Scharlab. Water used in all experiments was milliQ purity grade.

2.2. Catalyst preparation

CoTiAl layered double hydroxide (CoTiAl-LDH) was prepared following a solvothermal procedure described in the literature [29]. In brief, 0.30 g (1 mmol) of Co$(NO_3)_2 \cdot 6 H_2O$, 0.09 g (0.25 mmol) of Al$(NO_3)_3 \cdot 9 H_2O$, 120 μL (0.25 mmol) of a 50 wt% aqueous solution of Ti (IV) bis(ammonium lactate)dihydroxide (2:0.5:0.5 metal ratio), and 0.24 g (4 mmol) of urea were dissolved in 40 ml of methanol. The resulting solution was transferred to a 100 ml stainless steel autoclave and heated at 120 °C for 24 h. After cooling down, the pale brown precipitate was filtered, washed with methanol, and dried in a desiccator under vacuum at room temperature. Reference sample CoTi-LDH was synthesized following the same procedure, but adding 240 μL (0.5 mmol) of the Ti precursor and in the absence of Al$(NO_3)_3 \cdot 9 H_2O$.

To prove the relevancy of spherical morphology in the photocatalytic activity, CoTiAl-LDH was also prepared by a modified method described in the literature that allows the synthesis of LDH constituted by the stacking of few layers (CoTiAl-FL) [30]. In brief, 0.50 g (1.67 mmol) of Co$(NO_3)_2 \cdot 6 H_2O$, 0.16 g (0.42 mmol) of Al$(NO_3)_3 \cdot 9 H_2O$ and 200 μL (0.42 mmol) of a 50 wt% aqueous solution of Ti(IV) bis(ammonium lactate)dihydroxide (2:0.5:0.5 metal ratio) were dissolved in 50 ml of milliQ water. 20 ml of this solution was added dropwise with the use of a Perfusor® from Braun (10 min, 120 ml/h) over a 23 vol% N, N-dimethylformamide (DMF) solution in water. The addition took place at 80 ºC, and at a pH value of 10, kept constant during the process by the simultaneous addition of a 0.25 M NaOH solution with a titrator. The resulting suspension was cooled down in an ice bath and centrifuged at 5000 rpm for 10 min, washing three times with a 1:1 in vol. water: ethanol mixture. After this process the solid was recovered and dried in a desiccator under vacuum.

Once dried, the obtained materials were calcined in a muffle furnace under air atmosphere at 400 °C for 6 h, with a heating rate of 1 °C/min. The resultant mixed oxides were denoted as CoTiAl-MO, CoTi-MO and CoTiAl-FLc.

2.3. Materials characterization

Powder X-ray diffraction (PXRD) patterns were collected on a Philips X'PERT diffractometer operating at 40 kV and 45 mA equipped with a graphite monochromator using the Cu Kα radiation (λ = 1.54178 Å) in the range 2θ = 5–90°. Field emission scanning electron microscopy (FESEM) images and energy dispersive X-ray (EDX) data were recorded on a Zeiss Ultra 55 apparatus equipped with an EDX detector. Lamellar cross-sections of the materials were produced using a focused ion beam (FIB) scanning electron microscope setup (Zeiss Auriga Compact) with Ga as ion beam source. Transmission electron microscopy (TEM) of those lamellar sections were obtained on a JEOL JEM 2100 F equipment. Diffuse reflectance UV–visible spectroscopy (DRS) was performed on a PerkinElmer Lambda 1050 spectrophotometer equipped with a Harrick Praying Mantis™ diffuse reflectance accessory. CO$_2$ adsorption isotherms at low pressure range and 0 °C were measured on a Micromeritics

ASAP 2010 instrument equipped with a liquid circulation thermostatic bath using approximately 300 mg of sample. Previously, samples were pretreated overnight at 100 °C in vacuum to remove any adsorbed water. Surface area measurements were calculated afterwards using the Dubinin-Astakhov equation [31]. X-ray photoelectron spectroscopy (XPS) data were collected using a SPECS spectrometer equipped with a Phoibos 150 MCD-9 detector employing a nonmonochromatic X-ray source (Al) operating at 200 W. XPS was calibrated against adventitious carbon C 1 s at 284.6 eV. H$_2$ temperature programmed reduction (H$_2$-TPR) measurements were conducted on a Micromeritics Autochem 2910 apparatus in the range 40–800 °C with a heating rate of 10 °C/min under a gas flow of 10% H$_2$ in Ar (50 ml/min). In situ XRD measurements were performed on PANanalytical EMPYREAN diffractometer equipped with a high-temperature chamber (Anton Paar XRK-900). A 10% H$_2$ in Ar gas flow of 60 ml/min was circulated through the sample. Data were collected on a PIXcel1D-Medipix3 detector, with a Ni filter in the diffracted beam, and using Cu Kα irradiation (λ_1 = 1.5406 Å, λ_2 = 1.5444 Å, I_2/I_1 = 0.5), 45 kV voltage and 40 mA intensity. Data recording was made in the 2θ range of 5–90° at different temperatures (25, 200, 300, 400, 800 and 30 °C after cooling down the system).

Electrochemical impedance spectroscopy (EIS) measurements were performed on a Gamry Interface 5000E potentiostat, using a three-electrode single compartment quartz cell. 0.1 M Na$_2$SO$_4$ was used as the electrolyte, and Pt and Ag/AgCl electrodes as counter and reference electrodes, respectively. The scanning frequency range was 0.01 Hz-100 kHz at 1 V vs Ag/AgCl. Working electrode was prepared by drop-casting of a suspension consisting of 10 mg of the catalyst, 170 μL of ethanol and 23 μL of a commercial perfluorinated Nafion® resin solution (10 wt%) onto a FTO glass electrode, over an area of 1 cm^2 (1×1 cm).

2.4. Photocatalytic tests

Photo-assisted CO$_2$ hydrogenation was carried out on a home-made fixed-bed tubular continuous flow reactor operating at atmospheric pressure. The catalyst (50 mg) was loaded onto a fused quartz frit fixed inside a borosilicate glass tubular reactor. The photocatalyst bed was about 1 mm thickness and 10 mm diameter in vertical position placed on the porous quartz frit. The glass tube reactor was heated by an electric heating ribbon wrapped around its external surface, with the temperature being controlled by a κ-type thermocouple. The volume before the photocatalyst was sufficiently large to allow gas preheating before being in contact with the photocatalyst. The sample was irradiated from the top by using a 300 Xe lamp (108 mW/cm^2) by introducing the optical fiber (spot size 10 mm diameter) inside a quartz tube mounted on the top of the tubular reactor ensuring uniform irradiation on the whole sample surface. Prior to irradiation, the photocatalyst and the system were pretreated under H$_2$ flow at 400 °C for 1 h. After activation, the photocatalyst was cooled down and stabilized at the corresponding test temperature (200, 250, 300 or 350 °C) and a gas flow of CO$_2$ + H$_2$ (1:1 ratio, 13 ml/min) was circulated at atmospheric pressure through it while irradiating in the full UV–vis wavelength range. Samples from the outlet stream were collected with a Hamilton syringe and CO$_2$ reduction products were analyzed using a gas chromatograph (Agilent 7890 A GC System) equipped with a Carboxen®-1010 PLOT Capillary GC column and a TCD detector, using He as the carrier gas. A schematic of this setup can be found in Scheme S1.

Reaction order for CO$_2$ and H$_2$ was determined with the same setup but keeping the flow of one of the gases constant and varying the other. For apparent quantum yield (A. Q. Y.) measurements, the reaction temperature was 200 ºC, at which the thermal hydrogenation is negligible. The measurements were carried out using narrow band pass filters centered at different wavelengths (365, 405, 550 and 650 nm) coupled to the lamp to achieve pseudo monochromatic light. Light intensity was measured with a calibrated photodiode. The A. Q. Y. were obtained by dividing the number of product molecules formed by the number of photons in % according to the formula:

$$A.Q.Y = \frac{number \quad of \quad molecules \quad of \quad product}{number \quad of \quad photons} \times n \times 100$$

where *number of molecules of product = moles of product ×* 6.022·10²³, *number of photons* $= \frac{total \quad energy}{energy \quad of \quad one \quad photon} = \frac{I \cdot A \cdot t}{hc/\lambda}$ and the value of n is 2 for CO and 8 for CH$_4$.

3. Results and discussion

3.1. Materials characterization

The LDH precursor was prepared using methanol as solvent and urea as slow ammonia release agent by solvothermal synthesis (120 °C, 24 h) using aluminum and cobalt nitrates and titanium bis(ammonium lactate)dihydroxide complex as Ti source. The use of this Ti complex as precursor improves the stability of Ti in solution, slowing down the formation of TiO$_2$ in methanol solvent. Trimetallic Ti-containing mixed oxide was obtained by calcination at 400 °C under air atmosphere of the corresponding LDH as precursor. Scheme 1 illustrates the synthetic procedure followed in the preparation of the trimetallic metal oxide.

PXRD of CoTiAl-LDH after the synthesis exhibits the expected diffraction patterns characteristic of these materials (Fig. 1a), although the peaks were notably broad indicating that the crystallinity of the material was not high. Peaks at 2θ values of 9.8 and 19.6° can be assigned to (00 l) peaks of typical nitrate-intercalated LDH materials (JCPDS-38–0715) [32]. Upon calcination of CoTiAl-LDH at 400 °C, the corresponding trimetallic mixed oxide (CoTiAl-MO) was formed. This is reflected in PXRD analysis by the disappearance of the peaks corresponding to LDH phase and the appearance of new peaks at 31.4, 36.8, 44.7, 59.5 and 65.0° that can be ascribed to the (220), (311), (400), (511) and (440) planes of Co$_3$O$_4$ spinel, respectively (JCPDS-74–2120) [33]. The fact that there are no signals that can be attributed to the presence of Al and Ti in the XRD suggests that those metals are accommodated inside the spinel structure substituting Co atoms (in the form of CoAl$_2$O$_4$ or Co$_2$TiO$_4$, both isostructural with Co$_3$O$_4$), or in the case of Ti are also constituting amorphous separated phases. It is worth commenting that the reported XRD patterns of CoAl$_2$O$_4$ and Co$_2$TiO$_4$ are almost coincident with that of Co$_3$O$_4$ [34,35], and the broadness of the XRD peaks recorded for CoTiAl-MO does not allow to conclude their presence or absence. The presence of Al and Ti in the solid should contribute to the low degree of crystallinity observed in the material. Reference materials CoTi-MO and CoTiAl-FLc show similar diffractograms, meaning all calcined materials share the same crystalline structure (see Fig. S1).

EDX analysis showed that the ratio of metal cations in the CoTiAl-LDH sample is similar to those of the precursors added to the synthesis solution (see Table 1). This ratio is maintained upon calcination of the LDH to obtain the corresponding CoTiAl-MO. The cationic ratios of the reference samples also determined by EDX is shown in Table S1.

Table 1 also lists the estimated surface area of both catalysts, which were measured in CO$_2$ at 0 °C after a pretreatment at 100 °C to remove any adsorbed water. Area values were calculated following the Dubinin-Astakhov model [31]. CO$_2$ adsorption was employed instead of N$_2$ due to the lower kinetic diameter of the former (330 pm) compared to the latter (364) [36], allowing a better diffusion of the gas, and resulting in higher surface area values. The increase in surface area observed upon calcination of LDH is due to the transformation of the LDH with a 2D morphology into a nanoparticulated mixed oxide. This surface area increase upon calcination of LDH has been also previously reported in the literature [37].

FESEM images of these materials reveal that the morphology of CoTiAl-LDH was constituted as spherical aggregates of 2D nanosheets distributed radially from the center (Fig. 1e). As it can be seen in Fig. 1f, calcination of the samples at relatively moderate temperature (400 °C) preserved this characteristic morphology. These spherical aggregates can be explained considering that trimetallic LDH nucleates at the center and grows towards the exterior of the sphere. Accordingly, it can be proposed that during the solvothermal synthesis, the Ti-lactate complex undergoes some oligomerization forming micelles or aggregates constituted by oligo-polymeric Ti species and remaining in suspension. During the course of the reaction, as urea decomposition occurs and the basicity of the medium increases, trimetallic CoTiAl-LDH starts to nucleate preferentially around the Ti-lactate aggregates, in which Ti is located, resulting in a spherical assembly of 2D LDH sheets. As the LDH sheets evolve, consuming Ti atoms, the nuclei of Ti-lactate become smaller and finally disappears as evidenced by TEM images. PXRD patterns (Fig. S2), SEM images (Fig. S3a) and EDX analysis (Table S2) obtained at shorter synthesis times support this hypothesis, as in 2 h synthesis only spherical particles composed mainly by Ti and O without any LDH sheets can be observed. Longer synthesis times allow to observe nascent small nanosheets developing on the surface of the spherical Ti particles.

To provide more information about the spheres inner structure, lamellar cross-sections of the materials were cut using a FIB-SEM equipment. TEM images combined by elemental analysis by EDX of these cross-sections confirmed the spherical shape of 2D LDH aggregates (Fig. 1). High resolution TEM images show a basal spacing of 0.24 nm, which can be assigned to (311) facet of Co$_3$O$_4$ in agreement with XRD data (see supporting information for the correlation between the TEM spacing and 2θ angle in XRD). Elemental mapping of the samples shows the presence of Ti-rich regions near the nucleus of spheres with a lesser
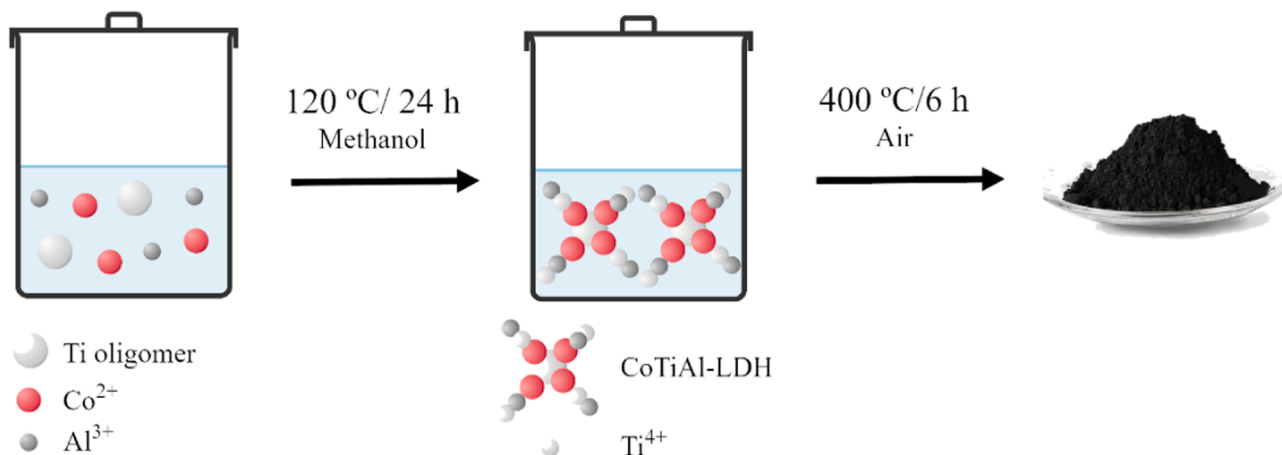
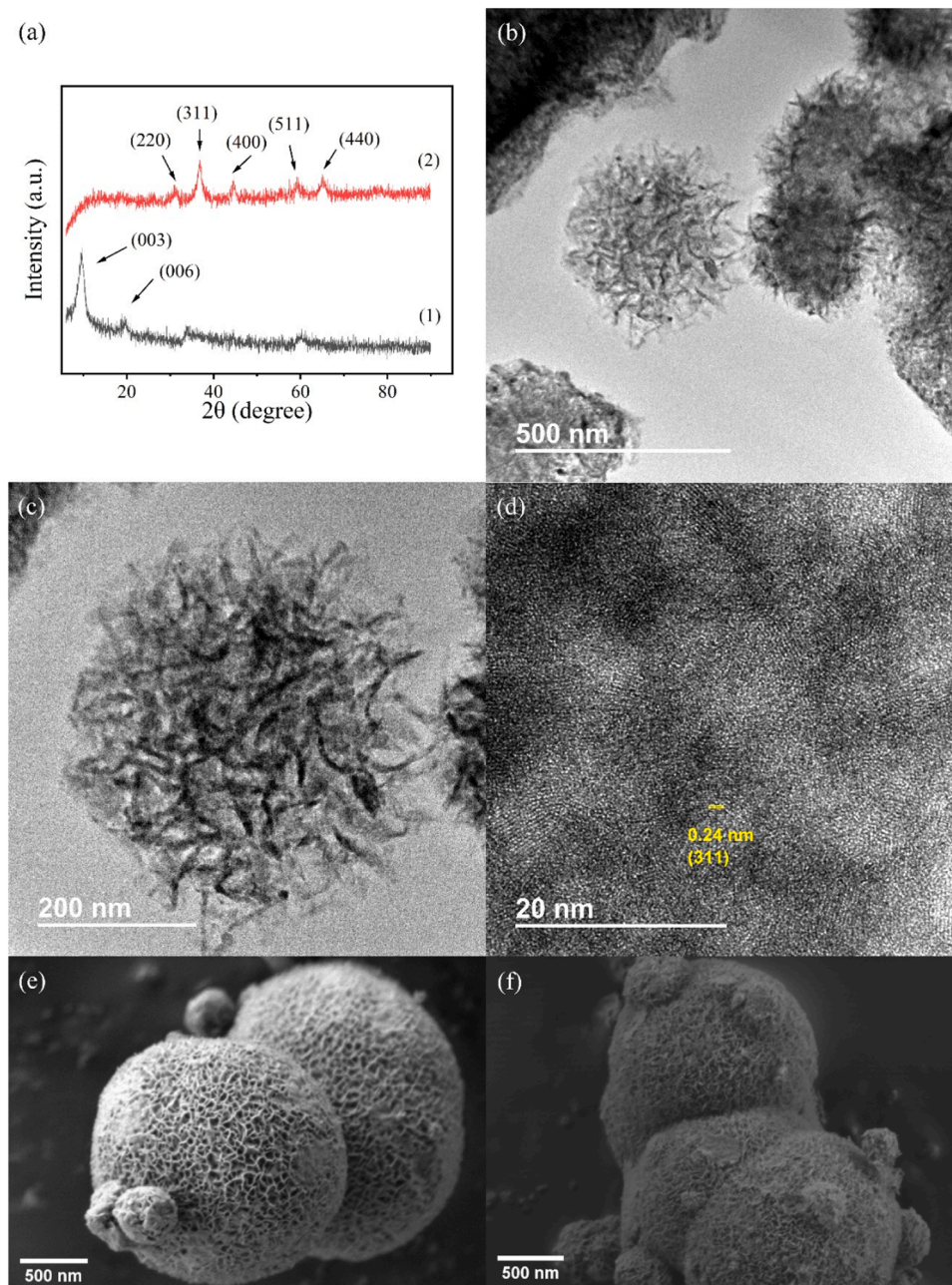**Scheme 1.** Synthetic procedure for the obtention of CoTiAl-MO.

Fig. 1. XRD patterns (a) of CoTiAl-LDH (1) and CoTiAl-MO (2). TEM images of CoTiAl-MO at different magnifications (b-d). SEM images of CoTiAl-LDH (e) and CoTiAl-MO (f).

Table 1
EDX and surface area values for CoTiAl-LDH and CoTiAl-MO.

	MATERIAL	
	CoTiAl-LDH	CoTiAl-MO
Co (%)	62.0	63.0
Ti (%)	19.4	18.5
Al (%)	18.6	18.5
Metal Ratio	1.6:0.5:0.5	1.7:0.5:0.5
Specific surface area (m^2/g)	62.8	224.1

degree of evolution on 2D LDH nanosheets (Fig. S3). This nucleus shows a contrast with the 2D sheets evolving from it, whose EDX analysis shows the presence of Co, Ti, and Al in the composition of the small nanosheets.

Morphological analysis of reference samples by electron microscopy showed that CoTi-MO also presented a sphere-like morphology, although the surface is decorated with rods instead of sheets. On the other hand, CoTiAl-FLc showed a nanosheet morphology with no spherical aggregation. Fig. S4 presents some images for these reference materials.

The elemental composition of the surface and the distribution of the metallic elements into different oxidation states and coordination spheres were analyzed by XPS (Fig. 2, Fig. S5). The presence of Co, Ti, Al, and O elements on the surface of both materials was confirmed by the survey XPS spectra. Ti 2p appears as two peaks corresponding to Ti $2p_{3/2}$ and Ti $2p_{1/2}$ at 458.0 and 463.6 eV attributable to Ti^{IV} [38]. A peak at 456.0 eV that could be assigned to a very small percentage of Ti^{III} [39] was inferred from the best deconvolution of the experimental XPS Ti$2p_{3/2}$ spectrum. In Co 2p XPS peak, the presence of two components at 780.6 and 782.4 eV, both attributable to Co^{II} in Co(OH)$_2$, and the
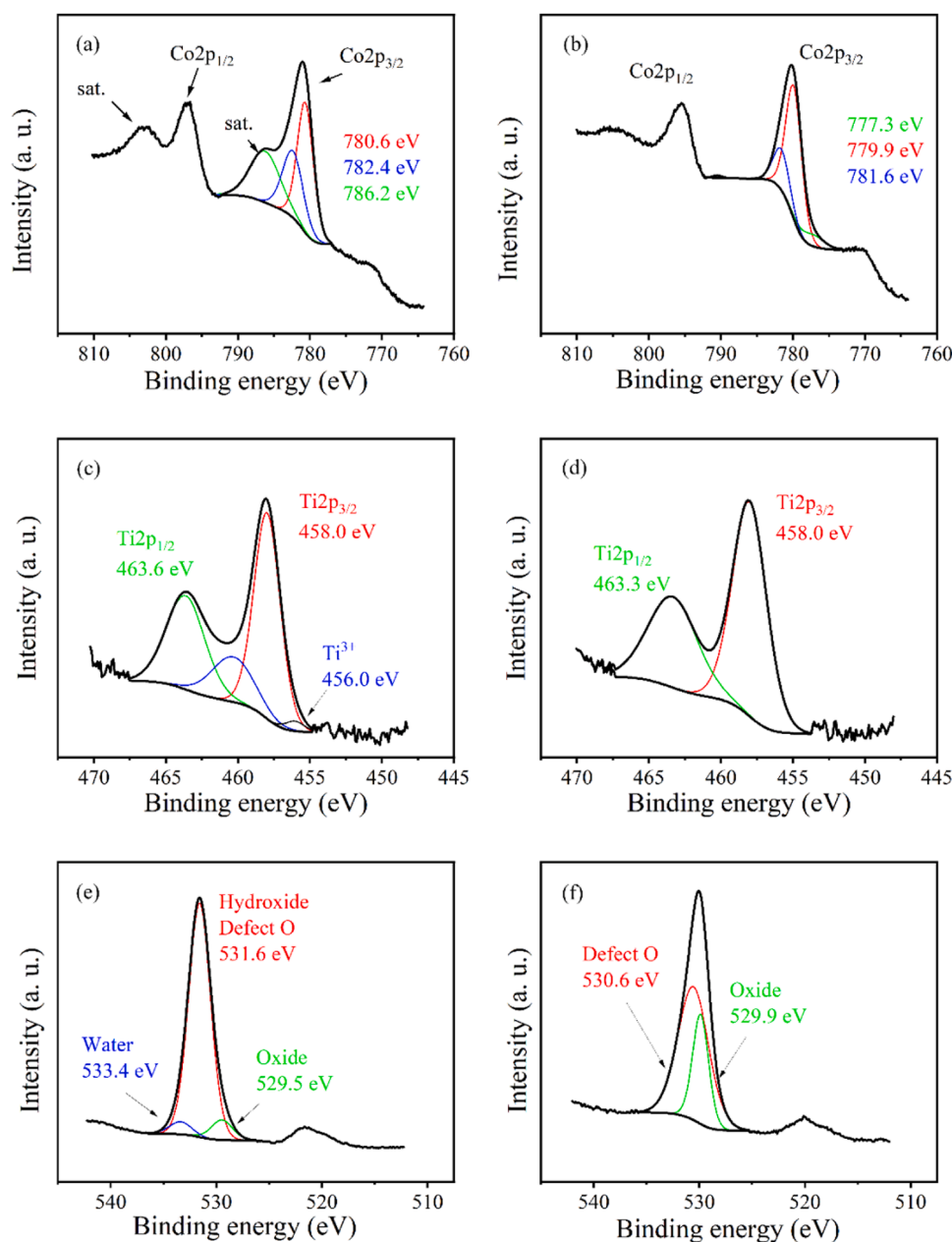
Fig. 2. Co2p XP spectra of CoTiAl-LDH (a) and CoTiAl-MO (b). Ti2p XP spectra of CoTiAl-LDH (c) and CoTiAl-MO (d). O1s XP spectra of CoTiAl-LDH (e) and CoTiAl-MO (f).

corresponding satellite at 786.2 eV was observed. According to the literature, in the case of Co 2p XPS peak, it is not possible to assign the deconvoluted components to a certain oxidation state or coordination sphere [40]. Al 2p spectra agrees with typical Al^{III} configuration, showing a single component at 73.9 eV [41]. O 1 s XPS can be deconvoluted in three components at 529.5, 531.6 and 533.4 eV, corresponding to oxygen atoms as oxide, hydroxide/oxygen next to vacancies, and adsorbed water, respectively [23,42]. After calcination and transformation of trimetallic LDH into the corresponding mixed oxide, a single Ti $2p_{3/2}$ component at 458.0 eV due to Ti^{IV} was observed in the high resolution XPS of Ti. In the case of Co, the mixed oxide presents two components at 781.6 and 779.9 eV, typical of Co atoms in Co_3O_4 structure. The most notable feature of Co $2p_{3/2}$ is the absence of the satellite peak observed in the LDH. This feature has been already reported in the literature for other related cobalt oxides [43] and can be attributed to the presence of Co in 2 different oxidation states, similarly to what has been reported in the case of Cu to explain the disappearance

of Cu 2p satellite bands [44]. Al 2p XPS shows a single-component peak at 73.2 eV, attributable to Al^{III}. Regarding O 1 s spectra, only two components at 529.9 and 530.6 eV could be observed and assigned to oxide and oxygen atoms next to vacancies, respectively. It should be noted that the component due to oxygen atoms next to vacancies has higher area than the oxide one, implying a high concentration of defects on the material, in concordance with other characterization techniques.

One property that is highly relevant in photocatalytic applications is the frontier band alignment. The optical band gap for trimetallic CoTiAl-LDH estimated from the Tauc plot of the diffuse reflectance UV-Vis spectrum considering the material as an indirect semiconductor was 2.59 eV. Upon calcination and transformation of LDH into trimetallic mixed oxide a noteworthy narrowing of the band gap derived from a remarkable shift of the absorption onset towards the NIR region was observed, giving a value of 1.31 eV. Fig. 3 provides a comparison of the diffuse reflectance UV-Vis-NIR absorption spectra of CoTiAl-LDH and CoTiAl-MO.
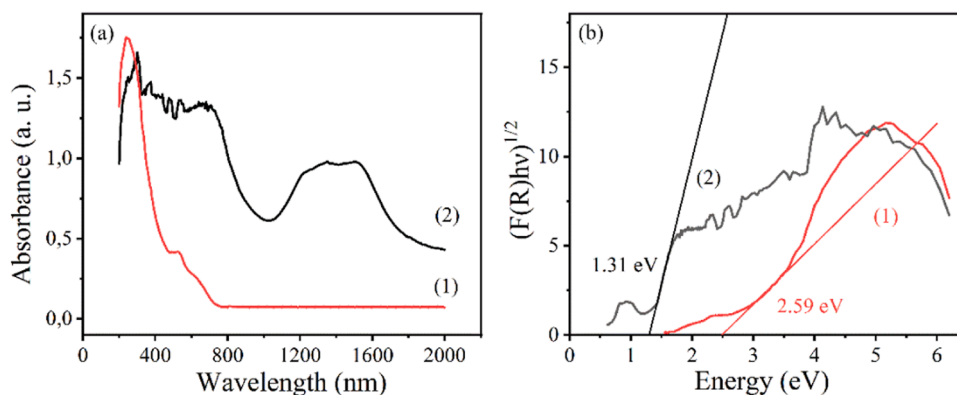
Fig. 3. Diffuse reflectance UV-Vis absorption spectra (a) and Tauc plots (b) of CoTiAl-LDH (1) and CoTiAl -MO (2) samples.

The ability to transfer electrons to the electrolyte was determined by EIS, observing notable changes in electrical properties between the LDH structure and the mixed oxide. Fig. 4 presents the Nyquist plots for the two materials. The smaller radius of the plot for CoTiAl-MO indicates smaller resistance for electron transfer between the solid and the surrounding electrolyte in comparison to the LDH structure [45]. In summary, both optical spectroscopy and electrochemical characterization indicate more favorable properties for its use as photocatalyst for CoTiAl-MO in comparison to CoTiAl-LDH regarding higher light harvesting and lower electron transfer resistance. In addition, the CoTiAl-MO better thermal stability, since this mixed oxide material is the resulting solid upon calcination, allows its use in those cases in which thermal assistance is required to overcome the activation barrier.

3.2. Photocatalytic activity for CO_2 reduction

As commented above, CoTiAl-MO should be the preferred catalyst for photocatalytic applications requiring certain temperatures due to the better thermal stability. The use of CoTiAl-LDH at temperatures of 200 ºC and above is not possible because it suffers a dihydroxylation process that transforms it into a mixed oxide. To prove the activity of CoTiAl-MO, photocatalytic CO_2 hydrogenation was carried out under continuous flow using a H_2/CO_2 ratio of 1:1 and a gas flow of 13 ml/min under UV-Vis light irradiation of the catalyst bed. First, the sample was pretreated at 400 °C under H_2 flow during 1 h. This pretreatment temperature was selected to ensure that the mixed oxide photocatalyst starts from the same phase at initial reaction time. Afterwards, the reactor temperature was set at the required reaction temperature. At these conditions, CO_2 conversion in two control experiments, either in the dark in presence of photocatalyst or under illumination in the absence of catalyst was negligible (<0.5%). In contrast, upon irradiation at 200 °C in the presence of CoTiAl-MO, a total product yield of 12% was
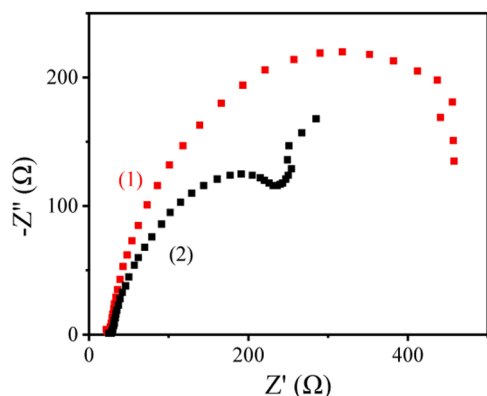
measured. The products formed were CO and CH_4 (72 and 28% selectivity, respectively) with no other products, particularly C_2 or CH_3OH, detected. When the continuous flow photoreaction was carried out a higher temperature in the range from 200 to 350 °C, higher CO_2 conversions and CO/CH_4 production rates were measured. Fig. 5 provides a comparison of the activity data for CO_2 hydrogenation in the dark and under irradiation, proving the occurrence of a photocatalytic process. As it can be seen in this Fig. 5, while at 200 °C the dark reaction is negligible, the thermocatalytic process increases exponentially with temperature and becomes notable at 300 °C and particularly at 350 °C. At this temperature, the thermocatalytic activity of CoTiAl-MO becomes more comparable to that of the analogous photocatalytic process. To put the photocatalytic activity of CoTiAl-MO in a broader context, Fig. S6 compares the CO production rate over CoTiAl-MO with some reference materials, while Table S3 provides a comparison of CoTiAl-MO performance with that of other catalysts previously reported for this reaction.

From the dependance of the product formation rate with the temperature, apparent activation energies for the thermocatalytic and photocatalytic reactions could be obtained by applying the Arrhenius equation [14,17]. It was found that the activation energies for the thermocatalytic reaction for CO and CH_4 were over 60 kJ/mol, while for the photocatalytic process these apparent activation energy values were much lower, about 10 kJ/mol. Fig. 5 also presents the Arrhenius plots from which the apparent activation energy values were determined, while Table S4 lists the corresponding activation energy values.

While the large contrast in activation energy reflects differences in the reaction mechanism, another kinetic measurement that has been frequently performed to establish the occurrence of different pathways between the thermal or photocatalytic process is the determination of the reaction order respect to the reactants. In the case of CoTiAl-MO these kinetic measurements are presented in Fig. 6 and were performed by keeping constant the reaction temperature and the flow of one of the reagents, while varying the flow of the other. The reaction order for each reactant and reaction conditions are also included in Table S4. It can be seen there that for both thermal and photocatalytic processes the reaction order was somewhat above 1 for CO_2, while it was below 1 for H_2. The similar reaction order for the thermal and photocatalytic processes, which are close to 1, would indicate that both CO_2 and H_2 are involved in the rate determining step and that the mechanism of the two processes require adsorption of both reagents as common step. The decrease in the reaction order for H_2 upon irradiation compared to the dark indicates a change in the reaction mechanism indicating that H_2 activation is less important for the rate determining step where photoinduced charge separation occurs.

It is important to note that even at 350 °C in where thermal reaction occurs in a substantial extent, conversion and product rates increase by a factor of 2 when the process is assisted by light of 108 mW·cm^{-2} power. This behavior has been previously well documented in the literature for photocatalytic CO_2 hydrogenation in which the relative increase of the
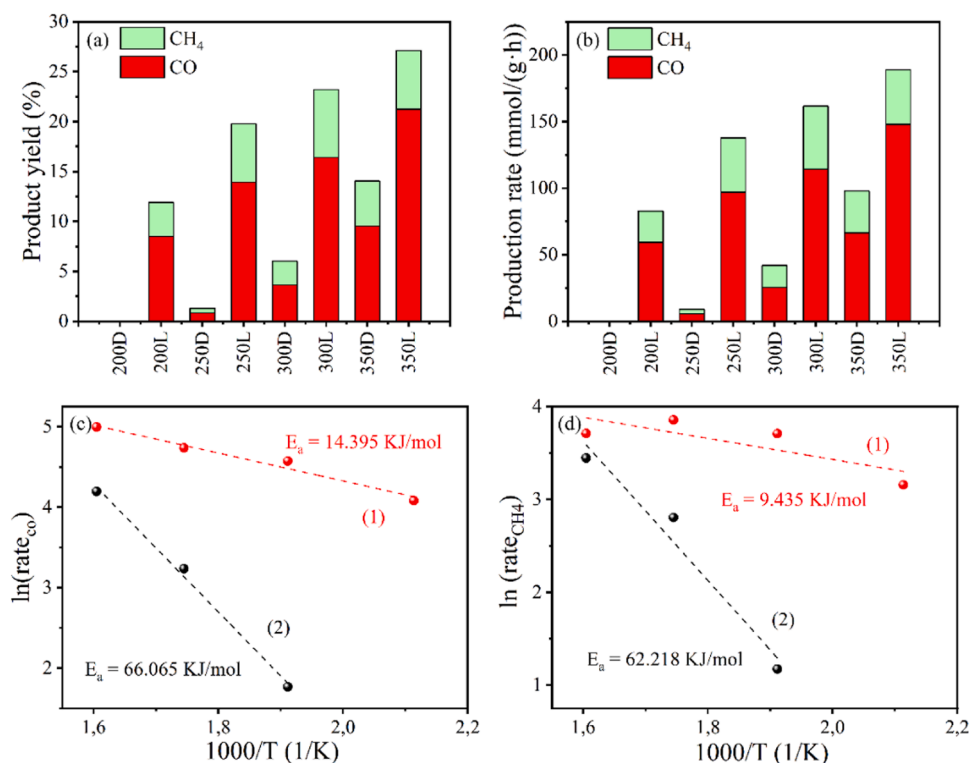

Fig. 4. Nyquist plots of CoTiAl-LDH (1) and CoTiAl-MO (2).

Fig. 5. Product yield (a) and rate (b) of CO and CH_4 in CO_2 hydrogenation over CoTiAl-MO photocatalyst. "L" stands for tests performed under irradiation and "D" for tests in dark conditions. Reaction conditions: $CO_2 + H_2$ flow (1:1 ratio, 13 ml/min), T: 200–350 ºC, UV-Vis irradiation (108 mW/cm^2), 50 mg photocatalyst. Arrhenius plots under illumination (1) and in dark conditions (2) for CO (c) and CH_4 (d) for the temperature range from 200 to 350 °C.
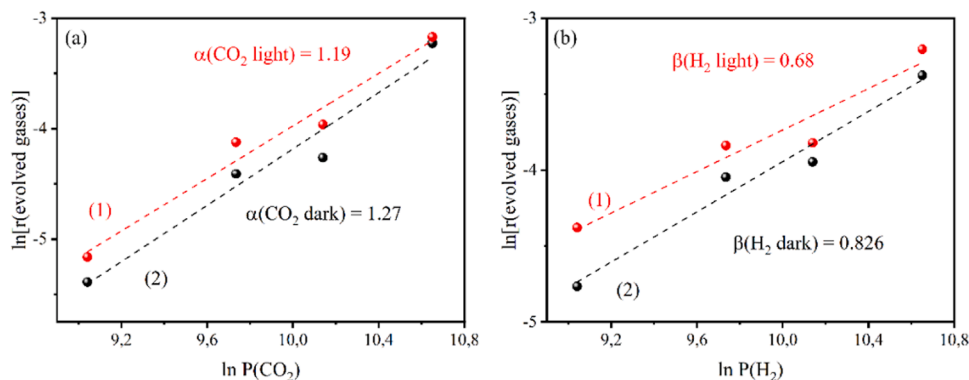

Fig. 6. Determination of the reaction order for CO_2 (a) and H_2 (b) in the dark and under illumination conditions. Reaction conditions: $CO_2 + H_2$ flow (different ratios, 13 ml/min), 200 °C, UV–vis irradiation (108 mW/cm^2), 50 mg photocatalyst. From these plots the following rate equation laws were deduced for lines (1): $r = k[CO_2]^{1.19}$ and $r = k[H_2]^{0.68}$; and lines (2) $r = k[CO_2]^{1.27}$ and $r = k[H_2]^{0.826}$.

product rate of the photocatalytic vs. the thermocatalytic process diminishes as the reaction temperature increases and thermal catalysis becomes more important as the temperature increases [46,47].

To determine the influence of light wavelength in the photocatalytic CO_2 reduction, apparent quantum yields for CO formation were determined in the range from 350 to 650 nm. These measurements were performed at a temperature of 200 °C because, as shown in Fig. 5, the thermal catalytic process is negligible at this temperature and therefore product evolution at this temperature requires photon absorption. The results are presented in Fig. 7. As it can be seen there, an apparent quantum yield of 7% was measured at 365 nm, while the photoresponse in the visible region was significantly lower, less than one order of magnitude than in the UV at 405 nm but increasing again towards the NIR region. It could be possible that the apparent quantum yield could be even higher at wavelengths shorter than 365 nm, however, the

current set up does not allow to monitor this UV region. Although apparent quantum yields in the visible are certainly low, they are measurable and much higher than those reported in other photocatalytic CO_2 reductions [48]. An estimation of the apparent quantum yield for CH_4 evolution gives a value of 4.6% at 365 nm. The fact that the A. Q. Y. dependence with the wavelengths do not follow the absorption spectrum of the CoTiAl-MO presented in Fig. 3 would indicate that this absorption spectrum corresponds of an envelope of various electronic transitions, some of which (those in the UV) are more efficient to promote CO_2 hydrogenation than others (those in the visible region). Deeper understanding of the optical spectrum is necessary to determine which electronic transitions are really involved in the photocatalytic process.

To prove the stability of the material, a long-term photocatalytic experiment was carried out. The results are shown in Fig. 8. As it can be seen there, the CO production rate does not decrease up to 108 h of
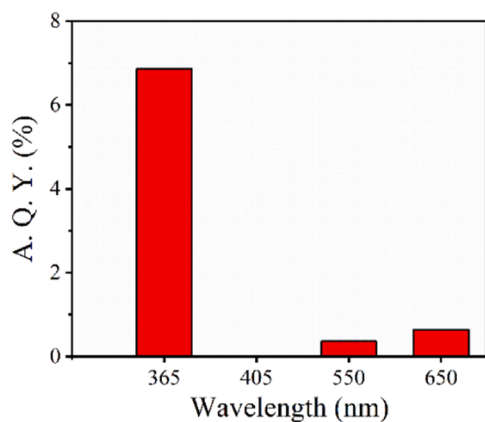
Fig. 7. Apparent quantum yield for CO production under different wavelength irradiation at 200 °C. Reaction conditions: CO_2 + H_2 flow (1:1 ratio, 13 ml/min), 200 °C, UV–vis irradiation (108 mW/cm^2, band pass filters centered at 365, 405, 550 and 650 nm), 50 mg photocatalyst.
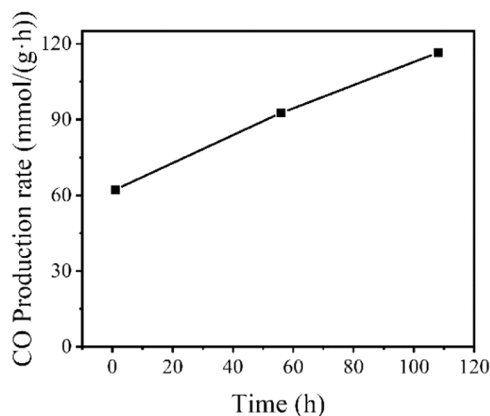

Fig. 8. CO production rate over CoTiAl-MO photocatalyst in long-term photocatalytic reaction. Reaction conditions: CO_2 + H_2 flow (1:1 ratio, 13 ml/min), T: 200ºC, UV-Vis irradiation (108 mW/cm^2), 50 mg photocatalyst.

photocatalytic reaction, moreover, it increases. This increase could be due to the liberation of active sites on the surface and pores of the material, that would be initially blocked. In addition, PXRD and SEM analysis of the samples after this long-term experiment was performed. The XRD pattern of the material after the test shows the characteristic peaks of the CoO phase, formed during pretreatment at 400 ºC under H_2 atmosphere, as well as a LDH peak at 2θ value of 11.8º, as presented in Fig. S7. This LDH phase can be originated by rehydration of a small fraction of the photocatalyst with the water generated in the photocatalytic reaction. The poor crystallinity of the material allows the observation of this new crystalline phase. As it can be seen in Fig. S8, the morphology of the material is retained.

With the information collected from all experimental data, some considerations about the reaction mechanism can be proposed. According to the literature, two possible mechanisms for the photocatalytic CO_2 hydrogenation could occur. One of them, termed as photothermal, consists in the conversion of photon energy into localized heat at the absorbing nanoparticle. This photothermal mechanism has been generally observed for metal nanoparticles responding in the whole spectral range, particularly in the NIR region. The second mechanistic pathway, applying mainly to semiconductors, involves charge separation with conduction band electrons reducing CO_2, that is simultaneously protonated, and H_2 becoming oxidized by the holes forming protons that are consumed in the CO_2 products. Assuming the operation of one of the two general mechanisms and based on the UV response of

the CoTiAl-MO photocatalyst, as well as the composition of the material for which we have not observed metallic particles, we propose that the most likely operating mechanism is the one involving charge separation. Scheme 2 illustrates our mechanistic proposal.

As commented earlier when describing the calcination of the CoTiAl-LDH into the trimetallic metal oxide, the obtained material possessed a very low degree of crystallinity. Nevertheless, the low intensity, broad peaks corresponding to Co_3O_4 change upon heating the catalyst at 300 °C under hydrogen atmosphere, becoming replaced by new signals corresponding to CoO. XRD profiles of CoTiAl-MO obtained under H_2 atmosphere at different temperatures are shown in Fig. S9. Although the poor crystallinity of the CoTiAl-MO does not allow to follow accurately its transformation under the reaction conditions, observation of the disappearance of the Co_3O_4 XRD peaks and its replacement by the diffraction pattern of CoO indicates that the photocatalyst could undergo a deep restructuration at 400 °C under pretreatment conditions. Worth noting at this point is that regardless the reaction temperature, all the irradiations were carried out at the required temperature after a previous activation step in which CoTiAl-MO was submitted at 400 ºC under H_2 flow for 1 h. Though, it is reasonable to assume that the presence of hydrogen and the activation temperature would favor reduction of Co^{III} into Co^{II}. This proposal is supported by H_2-TPR measurement (Fig. S10) of the photocatalyst that exhibits two peaks, one at 305 °C and the other at 640 °C indicating that hydrogen reacts with the material at these temperature ranges. The first peak with a hydrogen consumption area of 113.7 $\mu mol_{H2}/g$ would agree with the change of Co^{III} present in the mixed oxide into Co^{II}, and therefore, would be in accordance with the change in XRD pattern. The second hydrogen reduction peak at 640 °C with a significant larger hydrogen uptake corresponds to reduction of Co^{II} to Co^0. The amount of hydrogen uptake at 305 °C and 640 °C provides a quantitative estimation of the Co^{III} and Co^{II} content in the fresh photocatalyst and indicates that Co^{III} reduction must be occurring under the photocatalytic reaction conditions. Table S5 provides an estimation of Co^{II}/Co^{III} ratio in CoTiAl-MO obtained from H_2-TPR data.

4. Conclusions

A trimetallic CoTiAl LDH with a morphology of spherical aggregates of nanosheets has been synthesized. Characterization of the synthesis batch at different times indicates that nucleation of oligomeric Ti-lactate species as spherical particles is the fastest step occurring in the synthesis and the trimetallic CoTiAl-LDH starts to develop and grow from these initial Ti nuclei forming perpendicular petal-like aggregates. Thermal decomposition of CoTiAl-LDH at 400 °C affords the corresponding trimetallic CoTiAl mixed oxide that exhibits a remarkable photocatalytic activity for the continuous flow reverse water gas shift reaction at 200 °C, forming CO, accompanied by some CH_4. Although the same process can also take place in the dark with the assistance of heat, it requires higher temperatures about 350 °C to be comparable, being the dark thermocatalytic reaction negligible at 200 °C. The photocatalytic process has an apparent quantum yield at 200 °C for CO formation of 7% and a combined CO plus CH_4 yield of 11.6% that are remarkable values, among the highest in photocatalytic CO_2 reduction. The apparent activation energy values for CO and CH_4 formation in the 200–350 °C temperature range are also very low, about 10 kJ/mol that suggests a different mechanism compared to the thermocatalytic process. Overall, the present results show the potential that LDH materials offer for the preparation of multimetallic mixed oxides with high photocatalytic activity, allowing the combination of a wide chemical space of bi-, tri and tetravalent transition and main group metals. Further exploitation of this methodology using the optimal metal percentages should lead to further increase of the photocatalytic activity of multimetallic mixed oxides for CO_2 reduction.
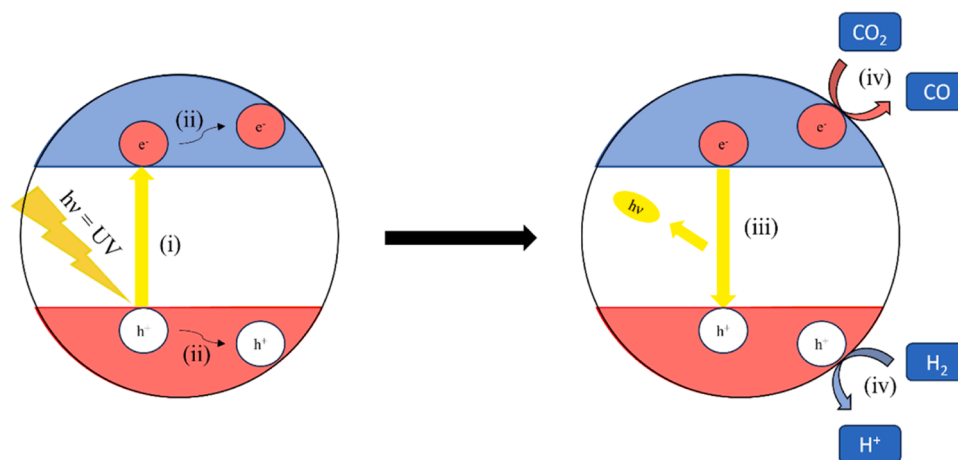
Scheme 2. Mechanistic proposal for photocatalytic CO_2 hydrogenation over CoTiAl-MO. In a first step (i), a UV photon is absorbed by the material, promoting an electron from the valence band to the conduction band, also generating a hole in the valence band. The generated charge carriers can move towards the surface of the photocatalyst (ii). In this process, electrons and holes can recombine, which results in the emission of a photon that can be observed in the photoluminescence measurements (iii). Another possibility is that charge carriers reach the surface of the photocatalyst and interact with CO_2 and H_2 molecules adsorbed there, transforming them in the reaction products by a redox reaction (iv).

CRediT authorship contribution statement

Yong Peng: Methodology, Investigation. **Horatiu Szalad:** Investigation, Data curation. **Antonio Ribera:** Writing – review & editing, Supervision, Funding acquisition. **Hermenegildo García:** Writing – review & editing, Supervision, Funding acquisition, Conceptualization. **Manuel Molina-Muriel:** Writing – original draft, Investigation, Data curation.

Declaration of Competing Interest

The authors declare that they have no known competing financial interests or personal relationships that could have appeared to influence the work reported in this paper.

Data availability

Data will be made available on request.

Acknowledgements

Appendix A. Supporting information

Supplementary data associated with this article can be found in the online version at doi:10.1016/j.jcou.2024.102725.

References

[1] N. Dewangan, W.M. Hui, S. Jayaprakash, A. Bawah, A.J. Poerjoto, T. Jie, A. Jangam, K. Hidajat, S. Kawi, Recent progress on layered double hydroxide (LDH) derived metal-based catalysts for CO2 conversion to valuable chemicals, Catal. Today 356 (2020) 490–513, https://doi.org/10.1016/j.cattod.2020.06.020.

[2] A. Rehman, G. Nazir, K.Y. Rhee, S. Park, Electrocatalytic and photocatalytic sustainable conversion of carbon dioxide to value-added chemicals: State-of-the-art progress, challenges, and future directions, J. Environ. Chem. Eng. 10 (2022) 108219, https://doi.org/10.1016/j.jece.2022.108219.

[3] X. Jiao, K. Zheng, L. Liang, X. Li, Y. Sun, Y. Xie, Fundamentals and challenges of ultrathin 2D photocatalysts in boosting CO2 photoreduction, Chem. Soc. Rev. 49 (2020) 6592–6604, https://doi.org/10.1039/D0CS00332H.

[4] P. Miao, J. Zhao, R. Shi, Z. Li, Y. Zhao, C. Zhou, T. Zhang, Layered Double Hydroxide Engineering for the Photocatalytic Conversion of Inactive Carbon and Nitrogen Molecules, ACS EST Eng. 2 (2022) 1088–1102, https://doi.org/10.1021/acsestengg.1c00489.

[5] J. Albero, Y. Peng, H. García, Photocatalytic CO2 Reduction to C2+ Products, ACS Catal. 10 (2020) 5734–5749, https://doi.org/10.1021/acscatal.0c00478.

[6] C. Lv, X. Bai, S. Ning, C. Song, Q. Guan, B. Liu, Y. Li, J. Ye, Nanostructured materials for photothermal carbon dioxide hydrogenation: regulating solar utilization and catalytic performance, ACS Nano 17 (2023) 1725–1738, https://doi.org/10.1021/acsnano.2c09025.

[7] X. Li, J. Yu, M. Jaroniec, X. Chen, Cocatalysts for selective photoreduction of CO2 into solar fuels, Chem. Rev. 119 (2019) 3962–4179, https://doi.org/10.1021/acs.chemrev.8b00400.

[8] Y. Zhou, A.J. Martín, F. Dattila, S. Xi, N. López, J. Pérez-Ramírez, B.S. Yeo, Long-chain hydrocarbons by CO2 electroreduction using polarized nickel catalysts, Nat. Catal. 5 (2022) 545–554, https://doi.org/10.1038/s41929-022-00803-5.

[9] Y. Qi, L. Song, S. Ouyang, X. Liang, S. Ning, Q. Zhang, J. Ye, Photoinduced Defect Engineering: Enhanced Photothermal Catalytic Performance of 2D Black In2O3−x Nanosheets with Bifunctional Oxygen Vacancies, Adv. Mater. 32 (2020) 1903915, https://doi.org/10.1002/adma.201903915.

[10] F. Chen, L. Zhou, C. Peng, D. Zhang, L. Li, D. Xue, Y. Yu, Bimetal-organic layer-derived ultrathin lateral heterojunction with continuous semi-coherent interfaces for boosting photocatalytic CO2 reduction, Appl. Catal. B, Environ. 331 (2023) 122689, https://doi.org/10.1016/j.apcatb.2023.122689.

[11] J. Zhao, R. Shi, G.I.N. Waterhouse, T. Zhang, Selective photothermal CO2 reduction to CO, CH4, alkanes, alkenes over bimetallic alloy catalysts derived from layered double hydroxide nanosheets, Nano Energy 102 (2022) 107650, https://doi.org/10.1016/j.nanoen.2022.107650.

[12] Z. Li, R. Shi, Y. Ma, J. Zhao, T. Zhang, Photodriven CO2 hydrogenation into diverse products: recent progress and perspective, J. Phys. Chem. Lett. 13 (2022) 5291–5303, https://doi.org/10.1021/acs.jpclett.2c01159.

[13] G. Fu, M. Jiang, J. Liu, K. Zhang, Y. Hu, Y. Xiong, A. Tao, Z. Tie, Z. Jin, Rh/Al Nanoantenna Photothermal Catalyst for Wide-Spectrum Solar-Driven CO2 Methanation with Nearly 100% Selectivity, Nano Lett. 21 (2021) 8824–8830, https://doi.org/10.1021/acs.nanolett.1c03215.

[14] C. Kim, S. Hyeon, J. Lee, W.D. Kim, D.C. Lee, J. Kim, H. Lee, Energy-efficient CO2 hydrogenation with fast response using photoexcitation of CO2 adsorbed on metal catalysts, Nat. Commun. 9 (2018) 1–8, https://doi.org/10.1038/s41467-018-05542-5.

[15] Y. Tang, Y. Wu, Y. Wang, L. Song, Z. Yang, C. Guo, J. Liu, F. Wang, Photo-Assisted Catalytic CO2 Hydrogenation to CO with Nearly 100% Selectivity over Rh/TiO2 Catalysts, Energy Fuels 37 (2023) 539–546, https://doi.org/10.1021/acs.energyfuels.2c03604.

[16] B. Deng, H. Song, Q. Wang, J. Hong, S. Song, Y. Zhang, K. Peng, H. Zhang, T. Kako, J. Ye, Highly efficient and stable photothermal catalytic CO2 hydrogenation to methanol over Ru/In2O3 under atmospheric pressure, Appl. Catal. B, Environ. 327 (2023) 122471, https://doi.org/10.1016/j.apcatb.2023.122471.

[17] Y. Peng, H. Szalad, P. Nikacevic, G. Gorni, S. Goberna, L. Simonelli, J. Albero, N. López, H. García, Co-doped hydroxyapatite as photothermal catalyst for selective CO2 hydrogenation, Appl. Catal. B, Environ. 333 (2023) 122790, https://doi.org/10.1016/j.apcatb.2023.122790.

[18] S. Singh, R. Verma, N. Kaul, J. Sa, A. Punjal, S. Prabhu, V. Polshettiwar, Surface plasmon-enhanced photo-driven CO2 hydrogenation by hydroxy-terminated nickel nitride nanosheets, Nat. Commun. 14 (2023) 1–18, https://doi.org/10.1038/s41467-023-38235-9.

[19] J. Zhao, Q. Yang, R. Shi, G.I.N. Waterhouse, X. Zhang, L. Wu, C. Tung, T. Zhang, FeO–CeO2 nanocomposites: an efficient and highly selective catalyst system for photothermal CO2 reduction to CO, NPG Asia Mater. 12 (2020) 1–9, https://doi.org/10.1038/s41427-019-0171-5.

[20] L. Wang, Y. Dong, T. Yan, Z. Hu, F.M. Ali, D.M. Meira, P.N. Duchesne, J.Y.Y. Loh, C. Qiu, E.E. Storey, Y. Xu, W. Sun, M. Ghoussoub, N.P. Kherani, A.S. Helmy, G. A. Ozin, Black indium oxide a photothermal CO2 hydrogenation catalyst, Nat. Commun. 11 (2020) 1–8, https://doi.org/10.1038/s41467-020-16336-z.

[21] G. Chen, R. Gao, Y. Zhao, Z. Li, G.I.N. Waterhouse, R. Shi, J. Zhao, M. Zhang, L. Shang, G. Sheng, X. Zhang, X. Wen, L. Wu, C. Tung, T. Zhang, Alumina-Supported CoFe Alloy Catalysts Derived from Layered-Double-Hydroxide Nanosheets for Efficient Photothermal CO2 Hydrogenation to Hydrocarbons, Adv. Mater. 30 (2018) 1704663, https://doi.org/10.1002/adma.201704663.

[22] Y. Zhao, Z. Li, M. Li, J. Liu, X. Liu, G.I.N. Waterhouse, Y. Wang, J. Zhao, W. Gao, Z. Zhang, R. Long, Q. Zhang, L. Gu, X. Liu, X. Wen, D. Ma, L. Wu, C. Tung, T. Zhang, Reductive Transformation of Layered-Double-Hydroxide Nanosheets to Fe-Based Heterostructures for Efficient Visible-Light Photocatalytic Hydrogenation of CO, Adv. Mater. 30 (2018) 1803127, https://doi.org/10.1002/adma.201803127.

[23] K. Bhattacharyya, G.P. Mane, V. Rane, A.K. Tripathi, A.K. Tyagi, Selective CO2 Photoreduction with Cu-Doped TiO2 Photocatalyst: Delineating the Crucial Role of Cu-Oxidation State and Oxygen Vacancies, J. Phys. Chem. C. 125 (2021) 1793–1810, https://doi.org/10.1021/acs.jpcc.0c08441.

[24] S. Song, H. Song, L. Li, S. Wang, W. Chu, K. Peng, X. Meng, Q. Wang, B. Deng, Q. Liu, Z. Wang, Y. Weng, H. Hu, H. Lin, T. Kako, J. Ye, A selective Au-ZnO/TiO2 hybrid photocatalyst for oxidative coupling of methane to ethane with dioxygen, Nat. Catal. 4 (2021) 1032–1042, https://doi.org/10.1038/s41929-021-00708-9.

[25] Y. Zhao, Y. Zhao, R. Shi, B. Wang, G.I.N. Waterhouse, L. Wu, C. Tung, T. Zhang, Tuning Oxygen Vacancies in Ultrathin TiO2 Nanosheets to Boost Photocatalytic Nitrogen Fixation up to 700 nm, Adv. Mater. 31 (2019) 1806482, https://doi.org/10.1002/adma.201806482.

[26] Y. Xu, Z. Wang, L. Tan, Y. Zhao, H. Duan, Y. Song, Fine Tuning the Heterostructured Interfaces by Topological Transformation of Layered Double Hydroxide Nanosheets, Ind. Eng. Chem. Res. 57 (2018) 10411–10420, https://doi.org/10.1021/acs.iecr.8b02246.

[27] Z. Wei, D. Feng, J. Li, Y. Lin, H. Zhang, Nanosheet array-like Cu@Cu.sub.2O-CuNiAl/rGO composites for highly efficient reduction of nitrophenol: Electronic and structure promotion effect of nickel, Chem. Eng. J. (Lausanne, Switz.: 1996) 427 (2022), https://doi.org/10.1016/j.cej.2021.131659.

[28] Y. Zhao, X. Jia, G. Chen, L. Shang, G.I.N. Waterhouse, L. Wu, C. Tung, D. O'Hare, T. Zhang, Ultrafine NiO Nanosheets Stabilized by TiO2 from Monolayer NiTi-LDH Precursors: An Active Water Oxidation Electrocatalyst, J. Am. Chem. Soc. 138 (2016) 6517–6524, https://doi.org/10.1021/jacs.6b01606.

[29] M. Molina-Muriel, Y. Peng, H. García, A. Ribera, Increased photocatalytic activity and selectivity towards methane of trimetallic NiTiAl-LDH, J. Alloy. Compd. 897 (2022) 163124, https://doi.org/10.1016/j.jallcom.2021.163124.

[30] J. Yu, B.R. Martin, A. Clearfield, Z. Luo, L. Sun, One-step direct synthesis of layered double hydroxide single-layer nanosheets, Nanoscale 7 (2015) 9448–9451, https://doi.org/10.1039/C5NR01077B.

[31] D.A. Cadenhead, J.F. Danielli, M.D. Rosenberg, Progress in Surface and Membrane Science, 1975.

[32] Rd.S. Macedo, R.B. Fazzi, A.Md.C. Ferreira, V.R.L. Constantino, Cobalt-based layered double hydroxides revisited: evidence for oxidizing radical generation, N. J. Chem. 44 (2020) 10022–10032, https://doi.org/10.1039/D0NJ00380H.

[33] W. Chen, B. Han, C. Tian, X. Liu, S. Liang, H. Deng, Z. Lin, MOFs-derived ultrathin holey Co3O4 nanosheets for enhanced visible light CO2 reduction, Appl. Catal. B, Environ. 244 (2019) 996–1003, https://doi.org/10.1016/j.apcatb.2018.12.045.

[34] F. Lv, W. Zhang, L. He, X. Bai, Y. Song, Y. Zhao, 3D porous flower-like CoAl2O4 to boost the photocatalytic CO2 reduction reaction, J. Mater. Chem. A 11 (2023) 2826–2835, https://doi.org/10.1039/D2TA08947E.

[35] Q.S. Fu, C.L. Li, B. Meng, C. Chakrabarti, R. Zhang, X.H. Chen, Y.H. Li, S.L. Yuan, Effect of annealing temperature on structural and magnetic properties of Co2TiO4 ceramics prepared by sol-gel method, Ceram. Int. 45 (2019) 6906–6911, https://doi.org/10.1016/j.ceramint.2018.12.187.

[36] A. Primo, A. Rendón-Patiño, C. Bucur, A. Jurca, B. Cojocaru, V.I. Parvulescu, H. Garcia, Doped microporous graphitic carbons as metal-free catalysts for the selective hydrogenation of alkynes to alkenes, J. Catal. 405 (2022) 355–362, https://doi.org/10.1016/j.jcat.2021.11.034.

[37] B. Kim, G. Gwak, T. Okada, J. Oh, Effect of particle size and local disorder on specific surface area of layered double hydroxides upon calcination-reconstruction, J. Solid State Chem. 263 (2018) 60–64, https://doi.org/10.1016/j.jssc.2018.03.041.

[38] M.C. Biesinger, L.W.M. Lau, A.R. Gerson, R.S.C. Smart, Resolving surface chemical states in XPS analysis of first row transition metals, oxides and hydroxides: Sc, Ti, V, Cu and Zn, Appl. Surf. Sci. 257 (2010) 887–898, https://doi.org/10.1016/j.apsusc.2010.07.086.

[39] Y. Zhao, B. Li, Q. Wang, W. Gao, C.J. Wang, M. Wei, D.G. Evans, X. Duan, D. O'Hare, NiTi-Layered double hydroxides nanosheets as efficient photocatalysts for oxygen evolution from water using visible light, Chem. Sci. 5 (2014) 951–958, https://doi.org/10.1039/C3SC52546E.

[40] D. Cabrera-German, G. Gomez-Sosa, A. Herrera-Gomez, Accurate peak fitting and subsequent quantitative composition analysis of the spectrum of Co 2p obtained with Al Kα radiation: I: cobalt spinel, Surf. Interface Anal. 48 (2016) 252–256, https://doi.org/10.1002/sia.5933.

[41] F. Lv, W. Zhang, L. He, X. Bai, Y. Song, Y. Zhao, 3D porous flower-like CoAl2O4 to boost the photocatalytic CO2 reduction reaction, J. Mater. Chem. A 11 (2023) 2826–2835, https://doi.org/10.1039/D2TA08947E.

[42] M.C. Biesinger, B.P. Payne, L.W.M. Lau, A. Gerson, R.S.C. Smart, X-ray photoelectron spectroscopic chemical state quantification of mixed nickel metal, oxide and hydroxide systems, Surf. Interface Anal. 41 (2009) 324–332, https://doi.org/10.1002/sia.3026.

[43] M.C. Biesinger, B.P. Payne, A.P. Grosvenor, L.W.M. Lau, A.R. Gerson, R.S.C. Smart, Resolving surface chemical states in XPS analysis of first row transition metals, oxides and hydroxides: Cr, Mn, Fe, Co and Ni, Appl. Surf. Sci. 257 (2011) 2717–2730, https://doi.org/10.1016/j.apsusc.2010.10.051.

[44] M.C. Biesinger, Advanced analysis of copper X-ray photoelectron spectra, Surf. Interface Anal. 49 (2017) 1325–1334, https://doi.org/10.1002/sia.6239.

[45] J. Li, Y. Xu, Z. Ding, A.H. Mahadi, Y. Zhao, Y. Song, Photocatalytic selective oxidation of benzene to phenol in water over layered double hydroxide: A thermodynamic and kinetic perspective, Chem. Eng. J. (Lausanne, Switz.: 1996) 388 (2020) 124248, https://doi.org/10.1016/j.cej.2020.124248.

[46] C. Wang, S. Fang, S. Xie, Y. Zheng, Y.H. Hu, Thermo-photo catalytic CO2 hydrogenation over Ru/TiO2, J. Mater. Chem. A 8 (2020) 7390–7394, https://doi.org/10.1039/C9TA13275A.

[47] N.T. Nguyen, M. Xia, P.N. Duchesne, L. Wang, C. Mao, F.M. Ali, T. Yan, P. Li, Z. Lu, G.A. Ozin, Enhanced CO2 Photocatalysis by Indium Oxide Hydroxide Supported on TiN@TiO2 Nanotubes, Nano Lett. 21 (2021) 1311–1319, https://doi.org/10.1021/acs.nanolett.0c04008.

[48] B. Tahir, M. Tahir, M.A. Che Yunus, A.R. Mohamed, A. Siraj, A. Fatehmulla, 2D/2D Mt/m-CN composite with enriched interface charge transfer for boosting photocatalytic CO2 hydrogenation by H2 to CH4 under visible light, Appl. Surf. Sci. 520 (2020) 146296, https://doi.org/10.1016/j.apsusc.2020.146296.